Chemical Science

Accepted Manuscript

This article can be cited before page numbers have been issued, to do this please use: Z. Gao, J. Liang, M. Sun, X. Yin, H. Ling, J. Wang, K. Wei, K. Li and W. Han, *Chem. Sci.*, 2026, DOI: 10.1039/D6SC02057G.

ROYAL SOCIETY OF CHEMISTRY

rsc.li/chemical-science

Surface engineering and local electron structure modulation to accelerate electroreduction of low-concentration nitrate

Zhifeng Gao[a], Jianxing Liang[b, c], Mingdi Sun[a], Xu Yin[a], Haojie Ling[a], Jiaxiu Wang[a], Kajia Wei[a], Kan Li[b]*, Weiqing Han[a]*

[a] Key Laboratory of Chemical Pollution Control and Resources Reuse, School of Environmental and Biological Engineering, Nanjing University of Science and Technology, Nanjing, 210094, Jiangsu Province, PR China

[b] State Key Laboratory of Green Papermaking and Resource Recycling, Shanghai Engineering Research Center of Solid Waste Treatment and Resource Recovery, School of Environmental Science and Engineering, Shanghai Jiao Tong University, 800 Dong Chuan Road, Shanghai, 200240, PR China

[c] School of Chemistry and Chemical Engineering, Shanghai Jiao Tong University, 800 Dong Chuan Road, Shanghai, 200240, PR China

*Corresponding authors.
E-mail addresses: likan@sjtu.edu.cn (K. Li), hwqnjust@aliyun.com (W. Han)

View Article Online
DOI: 10.1039/D6SC02057G

Abstract

Electroreduction of low-concentration nitrate is constrained due to the competitive hydrogen evolution side reaction and sluggish reaction dynamics. Herein, we present a NiFe-layered double hydroxide featuring hydrophobicity and oxygen vacancy by in-situ electrochemical intercalation of sodium dodecylbenzene sulphonate (V_O-NiFe-LDH/CF). Different of traditional intercalation by ion-exchange method, the V_O-NiFe-LDH/CF retains the hydrophobic property of the alkyl-chains in sodium dodecylbenzene sulphonate, while the sulfonic acid functional groups inhibit the formation of surface hydroxyl groups. The introduction of oxygen vacancy induces the local electron redistribution and d-band center optimization, thereby enhancing nitrate adsorption capacity and reducing energy barrier for the rate-determining step (*NO → *NOH). In situ FTIR measurement confirms the electrochemical hydrogenation route of nitrate. The optimized V_O-NiFe-LDH/CF can realize 96.8% nitrate removal efficiency and 96% ammonia selectivity at an initial NO_3^--N concentration of 50 mg L^{-1}. The NO_3^--N removal rate of V_O-NiFe-LDH/CF is 2.1-fold higher than that of NiFe-LDH/CF. Furthermore, V_O-NiFe-LDH/CF has excellent practicality for practical industrial nitrate-wastewater, the total nitrogen was reduced from 114.7 mg·L^{-1} to 7 mg·L^{-1}. The V_O-NiFe-LDH/CF shows outstanding stability and robust anti-interference performance during the long-term experiments.

Key Words: Layered double hydroxide, Hydrophobicity, Electroreduction, Oxygen vacancy, Low-concentration nitrate

View Article Online
DOI: 10.1039/D6SC02057G

1. Introduction

The electroreduction of nitrate to ammonia is a promising approach for sustainable nitrogen management, which is a "turning waste into wealth" strategy for ammonia production and the removal of NO_3^--N contamination [1, 2]. However, the electroreduction of low-concentration nitrate still suffers from competitive hydrogen evolution side reaction, particularly under acidic and neutral conditions. In addition, the process of nitrate convert to ammonia is inherently constrained due to the requirement of multi-electron/proton transfer and the high energy barrier of the hydrogenation step. The design of durable and efficient electrodes is crucial for the electroreduction of low-concentration nitrate.

Layered double hydroxide (LDH) is a promising electrocatalyst for various electrocatalytic reactions due to its low cost, scalable synthesis and tunable composition [3-6]. LDH is composed of positively charged brucite-like metal cation layers and the interlayer galleries with charge compensating anions and water molecule. The metal cations coordinated octahedrally by hydroxyl groups giving positively charged layers, each hydroxyl group is oriented toward the interlayer region and may be hydrogen bonded to the interlayer anions and water molecules. Interestingly, due to the relatively weak interlayer bonding of LDH, the controllable coordination environments of LDH can be constructed by regulating the interlayer molecules. However, most of works in previous researches focus on the modulation of interlayer spacing by various intercalation (e.g., polyoxometalates, biomolecules and metal complex anions) [4]. The NiFe LDH intercalated with dodecyl-sulfonate has exhibited stronger electrosynthesis activity for formaldoxime compared to that intercalated with Cl^-, in which the enhanced catalytic ability is attributed to the enlarged interlayer spacing of LDHs achieved by using different interlayer expansion agents [7]. The interlayer spacing of CoAl-LDH was enhanced from 0.76 to 1.33 nm by sodium dodecyl sulfate intercalated, and the enlarged interlayer spacing enhancing the ion-diffusion channel [8]. However, the mechanism of local electron redistribution by regulating the interlayer molecules of LDH is still unclear.

The water splitting reaction at the region of cathode has a significant impact on the electroreduction process of nitrate. The balance between the generation and consumption of atom hydrogen (*H) is crucial for the electrocatalytic hydrogenation of nitrate to ammonia [9, 10]. Electrode surface engineering plays a pivotal role in the design of catalysts, as it directly influences nitrate enrichment, proton-electron transfer kinetics and water splitting behavior on the electrode surface [11, 12]. Previous studies found that the hydrophobic interface significantly reduces H^+ concentration at the electrode surface compared to a hydrophilic interface, thereby effectively inhibiting HER and utilizing *H for hydrogenation of nitrate [13-16]. Liu *et al.* reported that controllable interfacial

wettability of CNT electrode by altering the lengths of the alkyl chains in the surfactant allows fewer interfacial water molecules to reach the CNT surface, thereby significantly inhibiting the competitive HER and promoting NH_3 selectivity [17]. Therefore, the development of LDH cathodes with hydrophobic surface by changing the interlayer molecules is a promising strategy for electroreduction of low-concentration nitrate.

In this work, we found that NiFe-LDH can obtain simultaneously the abundant oxygen vacancies and relatively hydrophobic surface only through adding the sodium dodecylbenzene sulphonate (SDBS) during the electro-deposition process (V_O-NiFe-LDH/CF). The alkyl-chains of SDBS contributes to the hydrophobic property, and the sulfonic acid functional groups of SDBS couple with metal cations inhibits the formation of surface hydroxyl groups, resulting in the formation of oxygen vacancies. The optimized V_O-NiFe-LDH/CF electrode achieved 96.8% nitrate removal efficiency and 96% ammonia selectivity at an initial NO_3^--N concentration of 50 mg L^{-1}. The nitrate removal rate of V_O-NiFe-LDH/CF is 2.1-fold higher than that of NiFe-LDH/CF without oxygen vacancies, while the hydrophobic electrode used in the traditional ion exchange method shows no significant improvement compared to NiFe-LDH/CF. This result indicated that the oxygen vacancies play an important role in the enhanced catalytic efficiency, and the hydrophobicity of the electrode reduces the accessibility of water molecules, thereby inhibiting the HER side reaction. The Bode phase plots and EPR spectra show that V_O-NiFe-LDH/CF maintains a good balance between generation and consumption of *H. The deoxygenation and hydrogenation process of electroreduction of nitrate was unveiled by in-situ FTIR spectra. Density functional theory (DFT) calculations revealed that the introduction of oxygen vacancy resulted in an optimized d-band center, enhanced nitrate adsorption capacity and reduced energy barrier of the rate-determining step (*NO to *NOH). Moreover, high N_2 selectivity (98.7%) was obtained in the presence of 1500 mg L^{-1} Cl^-. Furthermore, V_O-NiFe-LDH/CF has excellent practicality for practical industrial nitrate-wastewater, the total nitrogen was reduced from 114.7 mg·L^{-1} to 7 mg·L^{-1}. Consequently, the modulation of hydrophobicity and optimization of local electronic structure to enhance the conversion efficiency of nitrate to ammonia on the surface of electrode are highly effective. The unique design of a hydrophobic interface with oxygen vacancy synergy provides novel insights into regulating the nitrate-water interface environment and strategically designing advanced electrocatalysts for low-concentration nitrate wastewater treatment.

2. Experimental Section

2.1 Materials

All chemicals used in this work were bought from commercial suppliers and without further treatment. The detailed information is described in Text S1.

View Article Online
DOI: 10.1039/D6SC02057G

2.2 Preparation of the V_O-NiFe-LDH/CF

The NiFe-LDH with oxygen vacancy was prepared on the copper foam by the in-situ electrochemical intercalation method, and named V_O-NiFe-LDH/CF (Fig. 1a). Briefly, the electrodeposition electrolyte comprised 0.459 g $FeSO_4 \cdot 7H_2O$, 0.97 g $Ni(NO_3)_2 \cdot 6H_2O$, 0.213 g Na_2SO_4 and 0.03 g SDBS ($C_{18}H_{29}NaO_3S$) were dissolved in 50 mL deionized water. The electrodeposition process was carried out under the current density of 7.5 $mA \cdot cm^{-2}$ for 15 min in a two-electrode system where a commercial Ir-Ru/Ti and the CF were used as the counter electrode and working electrode, respectively. The prepared electrodes were repeatedly washed with deionized water and ethanol three times, and vacuum dried 12 h at 60 °C.

For control experiments, the NiFe-LDH/CF, V_O-Ni-LDH/CF and V_O-Fe-LDH/CF were prepared followed a similar procedure, except without the addition of SDBS, $FeSO_4 \cdot 7H_2O$ and $Ni(NO_3)_2 \cdot 6H_2O$, respectively. The NiFe-LDH/CF-SC and NiFe-LDH/CF-SDS were prepared followed a similar procedure, except replacing SDBS with sodium citrate (SC) and sodium dodecyl sulfate (SDS), respectively.

2.3 The experimental procedure of electrochemical nitrate reduction

The nitrate reduction experiments were carried out in a two-electrode system powered by a direct current power supply. The reaction tank was a 100 mL integrated electrolytic cell. As-prepared electrodes (2 × 3 cm^2) and the commercial Ir-Ru/Ti (2 × 3 cm^2) were employed as cathode and anode, respectively. The distance of two electrodes was set at 1.5 cm and 70 mL electrolyte including 50 mM Na_2SO_4 and 50 mg/L NO_3^--N, the reaction time 3 h. If not specified, the applied current density is 10 $mA \cdot cm^{-2}$. Subsequently, 1.0 mL of electrolyte was collected at 30 min interval and was quantitative determination according to colorimetric methods through the UV–vis absorption spectroscopy (Fig. S1) and the detailed measurement procedure is described in Text S2.

The NO_3^--N removal ratio, NH_4^+-N generation ratio and selectivity ($R_{NO_3^- - N}$, $G_{NH_4^+-N}$ and $S_{NH_4^+-N}$) were calculation by Eq. (1-3)

$$R_{NO_3^- - N}\ (\%) = \frac{[NO_3^-\text{-}N]_0 - [NO_3^-\text{-}N]_t}{[NO_3^-\text{-}N]_0} \times 100\% \quad (1)$$

$$G_{NH_4^+-N}\ (\%) = \frac{[NH_4^+\text{-}N]_t}{[NO_3^-\text{-}N]_0} \times 100\% \quad (2)$$

$$S_{NH_4^+-N}(\%) = \frac{[NH_4^+\text{-}N]_t}{[NO_3^-\text{-}N]_0 - [NO_3^-\text{-}N]_t} \times 100\% \quad (3)$$

Where $[NO_3^-\text{-}N]_0$ is the initial concentration (mg/L) of NO_3^--N. $[NO_3^-\text{-}N]_t$, $[NO_2^-\text{-}N]_t$, and $[NH_4^+\text{-}N]_t$ are the concentration (mg/L) of NO_3^--N, NO_2^--N and NH_4^+-N at time *t,* respectively. The other calculations are described in Text S3.

2.4 Characterizations and DFT calculations

View Article Online
DOI: 10.1039/D6SC02057G

The as-prepared electrodes were characterized by the X-ray photoelectron spectroscopy (XPS) X-ray diffraction (XRD), Fourier transform infrared spectrometer (FTIR), Raman microscopy, Scanning electron microscopy (SEM), Transmission electron microscopy (TEM) and Electron Paramagnetic Resonance (EPR). The electrochemical properties of electrodes were characterized used to the (CHI 660E, Chenhua) with three-electrode system with 50 mM $NaSO_4$ solution. The details are provided in the Supplementary material Text S4.

All the computations were conducted based on the density functional theory (DFT) using Vienna Ab Initio Simulation Package (VASP). The details are available in Text S5.

3. Results and discussion

3.1 Characterization of as-prepared cathodes

Fig. 1a illustrates the preparation process of V_O-NiFe-LDH on the Copper Foam (CF). All cathodes were prepared by constant-current electrodeposition process with a fixed current density. Compared to the synthesis of NiFe-LDH/CF, SDBS was strategically introduced as an intercalated agent during the electrodeposition of V_O-NiFe-LDH/CF to simultaneously enhance hydrophobicity and construct oxygen vacancies. In previous study, the SDBS was considered affect the growth of crystals due to the oriented aggregation based crystal growth [18]. The interaction between metal cations and surface hydroxyl groups is weakened due to the influence of the sulfonic groups of SDBS, resulting in the introduction of O vacancies in the LDH structure. As shown in Fig. 1b and 1c, the SEM images of NiFe-LDH reveal the nano-flower-like structure composed of single or multiple nanosheets stacked at 100-300 nm (Fig. 1d and 1e). The effect of morphology on catalytic performance was minimized in this study, in contrast to the finding reported by Wang *et al.* [8]. In addition, the nanosheets of V_O-NiFe-LDH exhibit a smoother surface compared to those of NiFe-LDH. The results demonstrate that the introduction of SDBS enhances the coordination with metal ions, thereby facilitating the formation of nanosheets. The TEM images further confirm the hierarchical nano-flower-like structure composed of stacked nanosheets (Fig. 1f and Fig. S2). The high-resolution (HR-TEM) image (Fig. 1g) of V_O-NiFe-LDH/CF and the corresponding fast Fourier transform (FFT) pattern, inverse FFT (IFFT) image and line profile (Fig. S3a-c) confirm that the lattice spacing (0.25 nm) corresponds to the (012) crystal planes of hydrotalcite-like structure. In addition, lattice stripe fractures and discontinuities (marked by yellow dotted lines) can be clearly seen, which may be attributed to oxygen vacancies [19]. Elemental mapping of V_O-NiFe-LDH/CF demonstrates the uniform distribution of Ni, Fe, S and O throughout the catalyst (Fig. 1h).

View Article Online
DOI: 10.1039/D6SC02057G

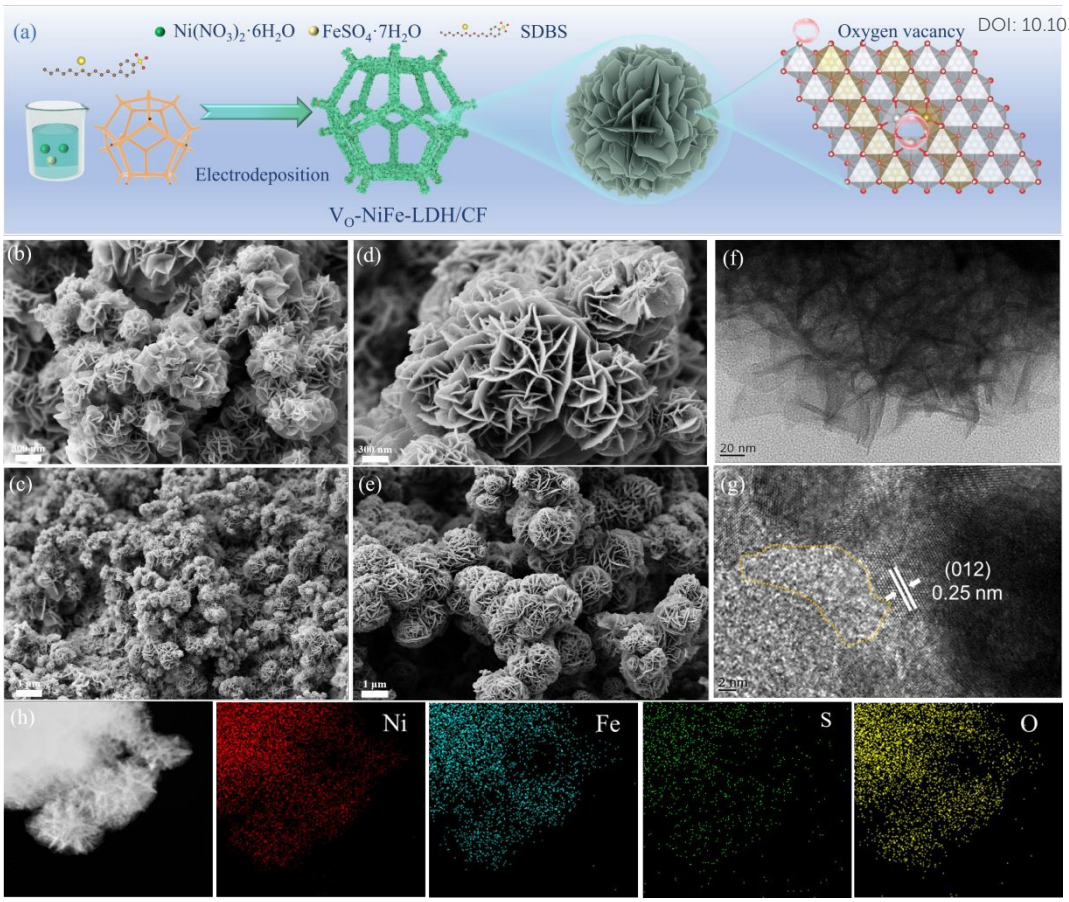

Fig. 1 (a) Schematic illustration of V_O-NiFe-LDH/CF synthesis route. (b, c) SEM images of NiFe-LDH/CF and (d, e) V_O-NiFe-LDH/CF at different resolution, (f, g) TEM image and HRTEM image, and (h) corresponding element mapping images of V_O-NiFe-LDH/CF.

As shown in Fig. S4, the diffraction peaks of metallic Cu at 2θ = 43.3°, 50.4° and 74.1° correspond to the CF substrate (PDF#04-0836) [20]. Additionally, XRD analysis of the sample scraped from the CF substrate confirms the formation of NiFe-LDH phase (Fig. 2a). The diffraction peaks located at 11.79°, 23.77°, 34.74°, 60.28° and 61.66° are indexed to the (003), (006), (012), (110) and (113) reflections of the hydrotalcite-like structure of LDHs, respectively, demonstrating the successful synthesis of NiFe-LDH [21]. The reduced crystallinity of V_O-NiFe-LDH/CF can be ascribed to the fact that the interaction between metal cations and sulfonic groups of SDBS inhibited the growth of the LDH. The (006) diffraction peaks at 23.77° of NiFe-LDH shifted to 22.6°, suggesting the intercalation of SDBS. According to the Bragg's Law[22], the d-spacing of A was calculated to be 0.75 nm and 0.79 nm, which confirming the intercalation effect of SDBS. The characteristic peaks at approximately 548 and 456 cm^{-1} in Raman spectroscopy of NiFe-LDH/CF (Fig. 2b), which correspond to the E_g bending mode and A_{1g} stretching mode of M-OH species in the NiFe-LDH [23, 24]. The shifted characteristic peaks were found in the V_O-NiFe-LDH/CF, which indicated the electron transfer between Ni and Fe. The FTIR spectra of as-prepared electrodes were collected in the range of 400 to 4000 cm^{-1} as shown in Fig. 2c. The characteristic peaks located at

3292 and 1627 cm^{-1} were identified as the stretching vibration of OH groups and the bending vibration of adsorbed water molecules, respectively [25]. The characteristic vibration bands at 2930 and 2856 cm^{-1} were observed, which are ascribed to the stretching vibration of the alkyl group in the long carbon chain structure of SDBS ions [26, 27]. The result further reveals the presence of SDBS intercalation anions in the interlayer space. XPS was employed to characterize the elemental composition and electronic states of the as-prepared electrodes. The survey spectrum (Fig. S5) of V_O-NiFe-LDH/CF displays distinct elemental signals for Cu 2p, Ni 2p, Fe 2p, O 1s, C 1s and S 2p, with the S 2p peak intensity notably higher than that of NiFe-LDH/CF. The characterization results confirm the successful growth of NiFe-LDH on the CF substrate, while the enhanced S 2p signal intensity further validates SDBS intercalation within the LDH interlayers [28]. The Ni 2p spectrum of NiFe-LDH/CF can be deconvolved into peaks of Ni^{2+} (855.42 and 872.94 eV) and Ni^{3+} (857.07 and 874.39 eV) and the along with satellite peaks at 861.67 and 878.97 eV, as shown in Fig. 2d. In Fig. 2e, the high-resolution Fe 2p XPS spectrum of NiFe-LDH/CF reveals two spin-orbit splitting peaks corresponding to Fe $2p_{3/2}$ and Fe $2p_{1/2}$, along with satellite peaks at 718.46 and 732.39 eV [23]. The peaks at 710.89 and 723.89 eV are ascribed to Fe^{2+}, while the peaks at 713.78 and 726.87 eV are assigned to Fe^{3+}. The peaks of Ni 2p and Fe 2p of V_O-NiFe-LDH/CF shift towards lower binding energy compared with that of the NiFe-LDH/CF. The negative shift in the binding energy of Ni 2p and Fe 2p implies changes in the electron distribution, which can be attributed to the delocalized electrons originating from oxygen vacancies [29]. As shown in Fig. 2f, the peaks at 529.8, 531.6 and 532.3 eV corresponded to the lattice oxygen (O_L), oxygen vacancies (O_V) with low coordination and hydroxy groups from surface-absorbed water molecules (O_A), respectively [30]. In the O 1s XPS spectrum, V_O-NiFe-LDH/CF demonstrated a comparatively lower proportion of O_L and a markedly higher intensity of O_V when compared to NiFe-LDH/CF. This observation suggests the generation of extra oxygen vacancies within the V_O-NiFe-LDH/CF electrode. Solid-state EPR was performed to further confirm the formation of oxygen vacancies. An obviously asymmetric signal at g=2.003 was observed after the addition of SDBS, which can be attributed to the unpaired electrons trapped in the oxygen vacancies (Fig. 2g). This finding further demonstrates the presence of oxygen vacancies [31]. Moreover, the S 2p spectrum of V_O-NiFe-LDH/CF is presented in Fig. S6. Furthermore, the specific surface area of as-prepared electrodes was investigated through N_2 adsorption-desorption experiments. The results indicated that V_O-NiFe-LDH/CF had a larger BET specific surface area compared to the other electrodes. In addition, the pore volume of the as-prepared electrodes was calculated and as shown in Fig. S7. It was observed that there was an increased proportion of mesopores. The increased BET specific surface area and pore volume facilitate ion adsorption kinetics and enhance ion diffusion, thereby improving mass transfer

View Article Online
DOI: 10.1039/D6SC02057G

efficiency [8]. The hydrophilicity of the electrodes was characterized by water contact angle measurements (Fig. 2i). The NiFe-LDH/CF electrode exhibited a water contact angle of nearly 0°, indicating its superhydrophilic property. After SDBS intercalation, the water contact angle of V_O-NiFe-LDH/CF increased to 137.8°, demonstrating a significant transition to hydrophobicity.

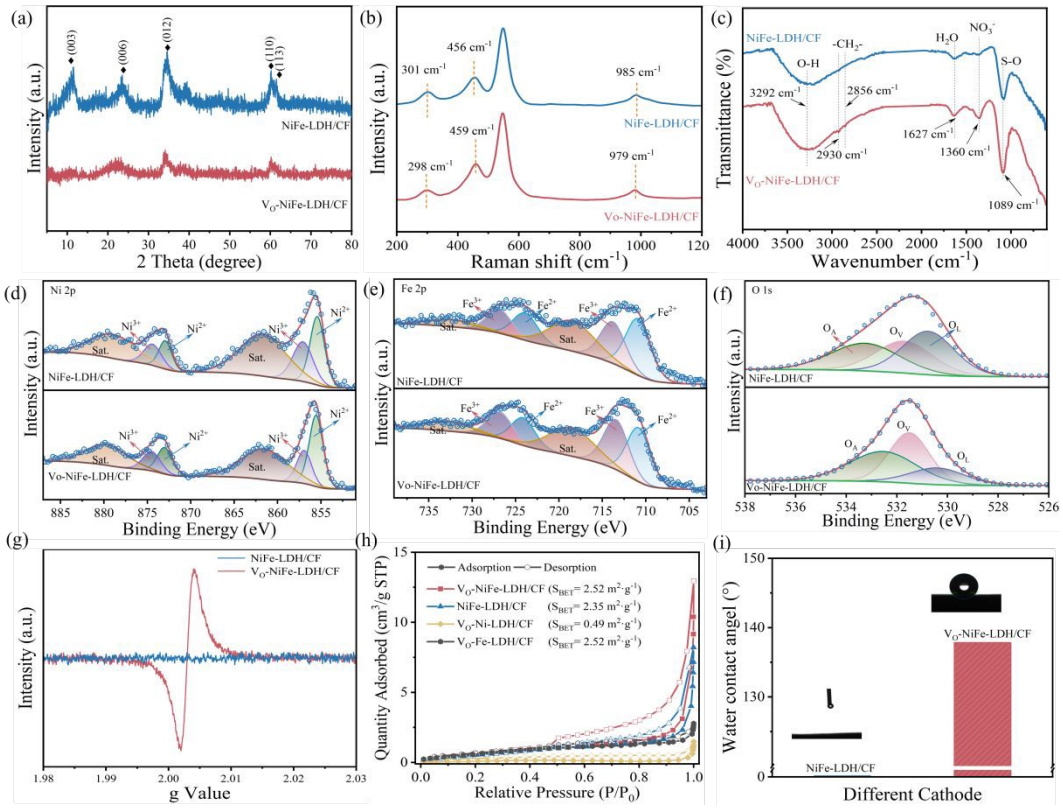

Fig. 2 (a) The XRD patterns, (b) Raman spectra, (c) FTIR spectra, (d-f) The Ni 2p, Fe 2p and O 1s XPS spectra, (g) EPR spectra, (h) N_2 adsorption-desorption isotherms of different electrodes and (i) Water contact angle of NiFe-LDH/CF and V_O-NiFe-LDH/CF.

3.2 Electrochemical nitrate reduction performance of as-prepared cathodes

The linear sweep voltammetry (LSV) curves of the V_O-NiFe-LDH/CF electrode are presented in Fig. 3a. A significantly increased current density and more positive onset potential were observed upon the addition of nitrate, demonstrating that nitrate electroreduction is preferentially promoted over HER on the V_O-NiFe-LDH/CF electrode surface. The LSV curves of different electrodes were evaluated in a 50 mM Na_2SO_4 electrolyte with NO_3^--N, further confirming the enhanced current response of V_O-NiFe-LDH/CF compared to other electrodes (Fig. S8). Additionally, the electrochemically active surface area (ECSA) analysis revealed that V_O-NiFe-LDH/CF possesses a higher double-layer capacitance (C_{dl}) of 43 mF · cm^{-2} than other electrodes, indicating a higher density of active sites after the introduction of oxygen vacancies (Fig. 3b and Fig. S9, S10). V_O-NiFe-LDH/CF exhibits a significantly lower Tafel slope than other electrodes, indicating faster reaction kinetics (Fig. S11). As shown in Fig. 3c and Fig. S12, electrochemical impedance

spectroscopy (EIS) results reveal the smallest charge transfer resistance for V_O-NiFe-LDH/CF, demonstrating its superior charge transfer efficiency compared to other electrodes. These electrochemical characterizations demonstrate that V_O-NiFe-LDH/CF exhibits the highest intrinsic catalytic activity among all prepared electrodes, indicating that the intercalation of SBDS effectively enhance the electrochemical activity of electrode. To further evaluate the nitrate reduction performance of the as-prepared electrodes, electrochemical nitrate reduction tests were conducted in a two-electrode system with a current density of 10 $mA \cdot cm^{-2}$, using an aqueous electrolyte containing 50 mM $NaSO_4$ and 50 $mg \cdot L^{-1}$ NO_3^--N. As shown in Fig. 3d-f, the CF substrate exhibits a negligible catalytic activity for NO_3^--N removal and NH_4^+-N generation, indicating that the contribution of substrate to nitrate-to-ammonia conversion is almost negligible in this reaction system. V_O-NiFe-LDH/CF exhibits a significantly higher NO_3^--N removal capacity (96.8% after 180 min of electrolysis) compared to other electrodes. Furthermore, the NO_3^--N removal rate for V_O-NiFe-LDH/CF (0.01375 min^{-1}) is 14.3, 6.5 and 2.1 times higher than those of V_O-Fe-LDH/CF (0.00096 min^{-1}), V_O-Ni-LDH/CF (0.00213 min^{-1}) and NiFe-LDH/CF (0.00656 min^{-1}), respectively. V_O-NiFe-LDH/CF exhibits excellent selectivity for NH_4^+-N (96%) and a lower generation ratio of NO_2^--N compared to other electrodes. It is noting that the generation ratio of NO_2^--N in V_O-NiFe-LDH/CF system maintains within a relatively lower range (Fig. S13). To avoid measurement error of UV–vis detection, we further performed ion chromatography (IC) tests on the same samples. As shown in Fig. S14, the results obtained from UV–vis and IC measurements are in good agreement, with only minor discrepancies between the two methods. To further investigate the stability of V_O-NiFe-LDH/CF, continuous electrolysis experiments with the V_O-NiFe-LDH/CF cathode are presented in Fig. 3g, and the NO_3^--N removal efficiency shows no significant attenuation during the 20 cycling experiments. Additionally, Ni and Fe leaching concentrations remained below 0.01 $mg \cdot L^{-1}$ throughout the operation, further confirming the excellent long-term stability of the V_O-NiFe-LDH/CF cathode (Fig. S15). After long-time cycling experiments, V_O-NiFe-LDH/CF hardly changed and still maintained a nano-flower-like structure (Fig. S16). Notably, post-reaction XPS results show that the relative concentration of oxygen vacancies decreases from 56.5% (Fresh electrode) to 48.8% (Used electrode) (Fig. S17). This phenomenon can be attributed to the adsorption of reaction intermediates, which increases the proportion of O_A and thus reduces the relative content of Ov. This result is consistent with the reported literature[32]. Furthermore, the XPS spectra of Fe 2p and Ni 2p show no obvious variation after long-term cycling experiments, further confirming the excellent structural stability of V_O-NiFe-LDH/CF. Additionally, compared with some reported electrodes by in-situ growth method, V_O-NiFe-LDH/CF exhibits a better performance in low-concentration nitrate removal under constant working current [33-39]. As shown

in Fig. 3h, the V_O-NiFe-LDH/CF has a stronger removal ability of NO_3^--N under relatively lower working current, which indicated that it may have promising industrial application prospects.

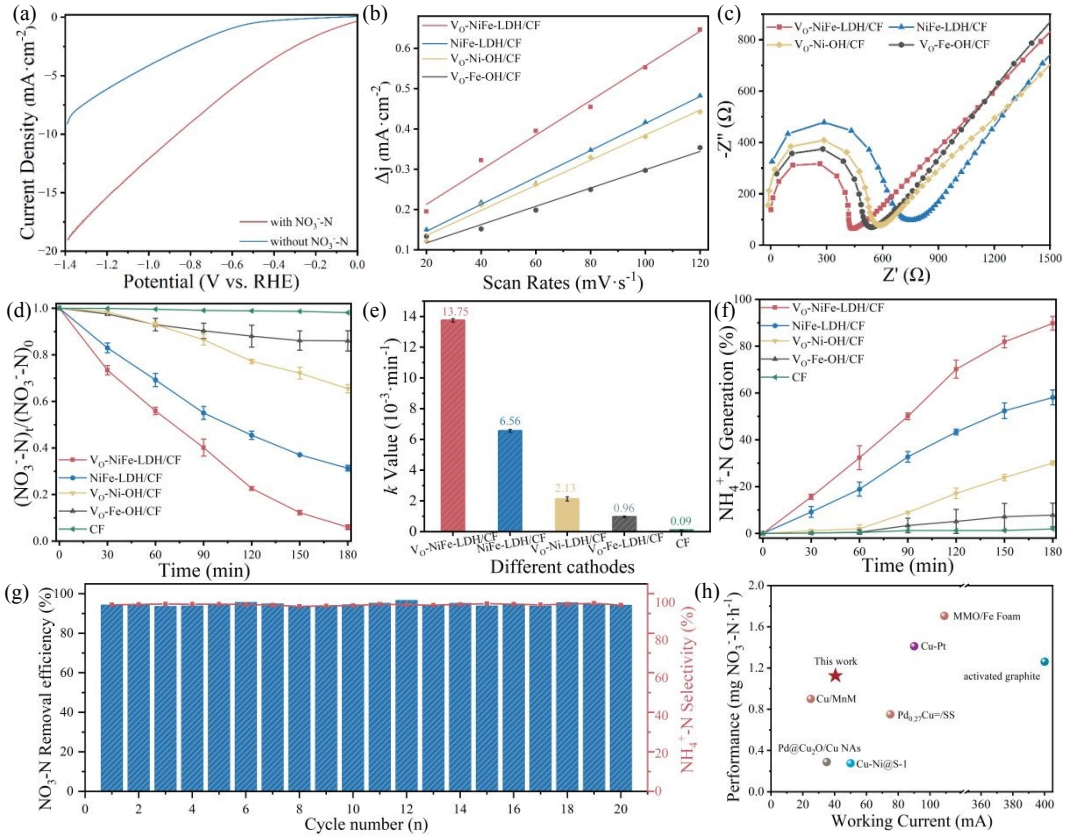

Fig. 3 (a) LSV curves of V_O-NiFe-LDH/CF with and without NO_3^--N, (b) Linear fitting of the capacitive properties of current density vs. scan rate (c) EIS Nyquist plots, (d-f) the performance (the removal ability and kinetic rate constant of NO_3^--N removal and NH_4^+-N generation ratio) of electrochemical nitrate reduction of different electrodes, (g) the stability tests and (h) Comparison of reported electrodes for low-concentration nitrate removal under constant working current.

3.3 Electroreduction Mechanism of Nitrate over V_O-NiFe-LDH/CF

In order to determine the role of oxygen vacancies and surface hydrophobicity in the electroreduction of nitrate, we have added two additional control electrodes. A hydrophilic LDH with comparable oxygen vacancy concentration (NiFe-LDH/CF-SC) was synthesized using sodium citrate (SC) as the intercalating agent, while a hydrophobic LDH without oxygen vacancies (NiFe-LDH/CF-SDS) was prepared with sodium dodecyl sulfate (SDS) as the intercalating agent. SC induces oxygen vacancies mainly through the chelation of its hydroxyl and carboxyl groups with metal ions of LDH. This interaction disturbs the local coordination environment and causes lattice distortion, thereby generating unsaturated coordination sites and eventually leading to the formation of oxygen vacancies. By contrast, SDS undergoes directional adsorption and hydrophobic self-assembly via its long alkyl chains, solely endowing the electrode with surface hydrophobicity.

Owing to the absence of strong electron-withdrawing groups that induce defect, SDS does not facilitate the formation of oxygen vacancies. The surface wettability and oxygen vacancy defects of the as-prepared electrodes were systematically characterized, as displayed in Fig. S18. As shown in Fig. S19, the V_O-NiFe-LDH/CF exhibits a higher removal capacity of NO_3^--N than other electrodes. Both NiFe-LDH/CF-SC and NiFe-LDH/CF-SDS also outperform NiFe-LDH/CF. Furthermore, the NiFe-LDH/CF-SC exhibits better catalytic performance than NiFe-LDH/CF-SDS, indicating that oxygen vacancies play a more dominate role than surface hydrophobicity in the electrocatalytic nitrate reduction process. The V_O-NiFe-LDH/CF exhibits a higher Faradaic efficiency (44.2%) and NH_3 yield rate than the other control electrodes (Fig. S20), and the energy consumption for NH_3 is 2.17 kWh/mol. To further investigate the catalytic mechanism of V_O-NiFe-LDH/CF, *Operando* EIS and DFT calculations were employed to study the reaction kinetics of water dissociation, nitrate activation and the reduction process [40-42]. Differential charge density analysis reveals stronger electron transfer at the V_O-NiFe-LDH and $*NO_3$ interfacial compared to NiFe-LDH (Fig. 4a), demonstrating that oxygen vacancy induces the local electron redistribution. The Bader charge analysis revealed that the V_O-NiFe-LDH transferred 0.39 electron equivalents to NO_3^-, significantly higher than the values for NiFe-LDH (0.25). In Fig. S21, the conversion efficiency of nitrate-to-ammonia is inhibited after the TBA adding. The control experiments by replacing H_2O with deuterium oxide (D_2O) to clarify the role of *H, since *H is originated from the electrochemical splitting of H_2O. The current densities of LSV curves decreased when D_2O was used instead of H_2O (Fig. S22a), and the kinetic isotope effect (KIE) value of V_O-NiFe-LDH/CF is 1.64 (Fig. S22b), demonstrating that *H plays a critical role in the electrochemical reduction of NO_3^--N. Furthermore, V_O-NiFe-LDH/CF exhibits stronger DMPO-*H adduct peaks than NiFe-LDH/CF, and the peak intensity decreases after the addition of nitrate, suggesting that V_O-NiFe-LDH/CF has an enhanced ability for *H generation and consumption (Fig. 4b). Fig. 4c presents the Bode phase plots of V_O-NiFe-LDH/CF under different working potentials. In the absence of nitrate, the Volmer step (water dissociation process) is the dominant reaction. The positive shift of peak position with increasing potential is observed, indicating enhanced water dissociation kinetics and increased *H generation. Upon application of a sufficiently large potential, the peak exhibits a distinct shift toward the middle frequency range, thereby accelerating the Heyrovsky step for HER [43]. After nitrate addition, significant decreases in peak intensity and notable shifts in peak position toward higher frequency

View Article Online
DOI: 10.1039/D6SC02057G

are observed, confirming that suppressed Heyrovsky step and generated *H species are preferentially consumed for nitrate reduction hydrogenation step compared to HER. In Fig. S23a, V_O-NiFe-LDH/CF exhibits a significantly lower peak intensity than NiFe-LDH/CF, with peaks shifting to higher frequency under increasingly negative applied potential. These results indicate that the Volmer step has achieved dynamic equilibrium, and H* generated from water dissociation is preferentially consumed at the V_O-NiFe-LDH/CF surface during the nitrate reduction, thereby promoting the hydrogenation of nitrate to ammonia [44]. Additionally, the peak position of V_O-NiFe-LDH/CF shifts toward lower frequency in the middle frequency range (10^0-10^2 Hz) compared with other electrodes, further confirming that oxygen vacancy introduction and bimetallic collaboration can effectively suppress Heyrovsky step, thereby inhibiting the HER side reaction (Fig. S23b). Furthermore, Fig. 4d presents the calculated projected density of states (PDOS) and corresponding d-band centers for V_O-NiFe-LDH (-2.29 eV) and NiFe-LDH (-3.08 eV), revealing distinct electronic structure differences induced by oxygen vacancies. A positively shift of d-band center for V_O-NiFe-LDH is closer to the Fermi level compared to NiFe-LDH, which is beneficial to the adsorption of nitrate and the intermediates[45]. The calculations of *H free energy on the different electrocatalysts (Fig. 4e) demonstrate enhanced adsorption ability of *H, thereby promoting the hydrogenation steps in nitrate-to-ammonia conversion. In situ FTIR spectra were collected to monitor the intermediates adsorbed on the surface of electrode (Fig. 4f and S24). The characteristic peak around at 1340 cm^{-1} could be attributed to the vibration of $*NO_3^-$ [42]. The characteristic peaks of the protonation intermediates were found, including –N–H (2850 and 2951 cm^{-1}) [46], *NH (1558 cm^{-1}) , *NHOH (1525 cm^{-1})[47, 48] and the product NH_4^+ (around 1457, 1507 cm^{-1}) [49], while the band at 1652 cm^{-1} is attributed to *NO [50]. The relative peak intensity ratio of *NHOH versus *NO species gradually increased with increasing working potential, demonstrating the hydrogenation pathway of nitrate reduction. Moreover, the ratio over V_O-NiFe-LDH/CF was significantly higher than that over NiFe-LDH/CF at the same working potential, further revealing the promoted hydrogenation kinetics. In addition, the adsorption free energy of the $NO_3^- \rightarrow *NO_3$ process, identified as the prerequisite rate-determining step in the overall nitrate reduction reaction. The adsorption energy of NO_3 decreases from 0.14 eV to -0.54 eV, indicating that the energy barrier of the prerequisite step is overcome and the reaction shifts toward a thermodynamically favorable spontaneous process. The enhanced nitrate adsorption ability of V_O-NiFe-LDH/CF was evaluated by electrochemical impedance-potential

spectra at different nitrate concentration (Fig. S25 and S26). The enhanced specific adsorption of NO_3^- on the V_O-NiFe-LDH/CF was proved according to the Esin-Markov effect on the inner Helmholtz plane [51]. The result is favor of the successive deoxidation and hydrogenation steps. The Gibbs free energy profiles of the nitrate to ammonia on NiFe-LDH and V_O-NiFe-LDH are presented in Fig. 4g. The nitrate to ammonia process can be considered as a direct reduction process in combination with electron transfer and N-H bonding. Nitrate reduction reaction proceeds through a series of intermediates with N valences ranging from +5 to -3: $NO_3^- \rightarrow *NO_3 \rightarrow *NO_2 \rightarrow *NO \rightarrow *NOH \rightarrow *NHOH \rightarrow *NH_2OH \rightarrow *NH_2 \rightarrow *NH_3 \rightarrow NH_3$. DFT calculations reveal that the $*NO \rightarrow *NOH$ step is the rate-determining step for NiFe-LDH in the whole process. The presence of oxygen vacancy reduces the reaction energy barrier of $*NO \rightarrow *NOH$ (0.23 eV) compared to NiFe-LDH/CF (0.35 eV). In summary, to address the HER competitive reactions and sluggish reaction dynamics associated with the removal of low-concentration nitrate, we proposed a strategy of adding SDBS during LDH electrode deposition to introduce oxygen vacancies. The strategy regulates the surface hydrophobicity and local electronic structure of the electrode, thereby enabling appropriate *H supply and reducing the energy barrier of the hydrogenation process (Fig. 4h).

View Article Online
DOI: 10.1039/D6SC02057G

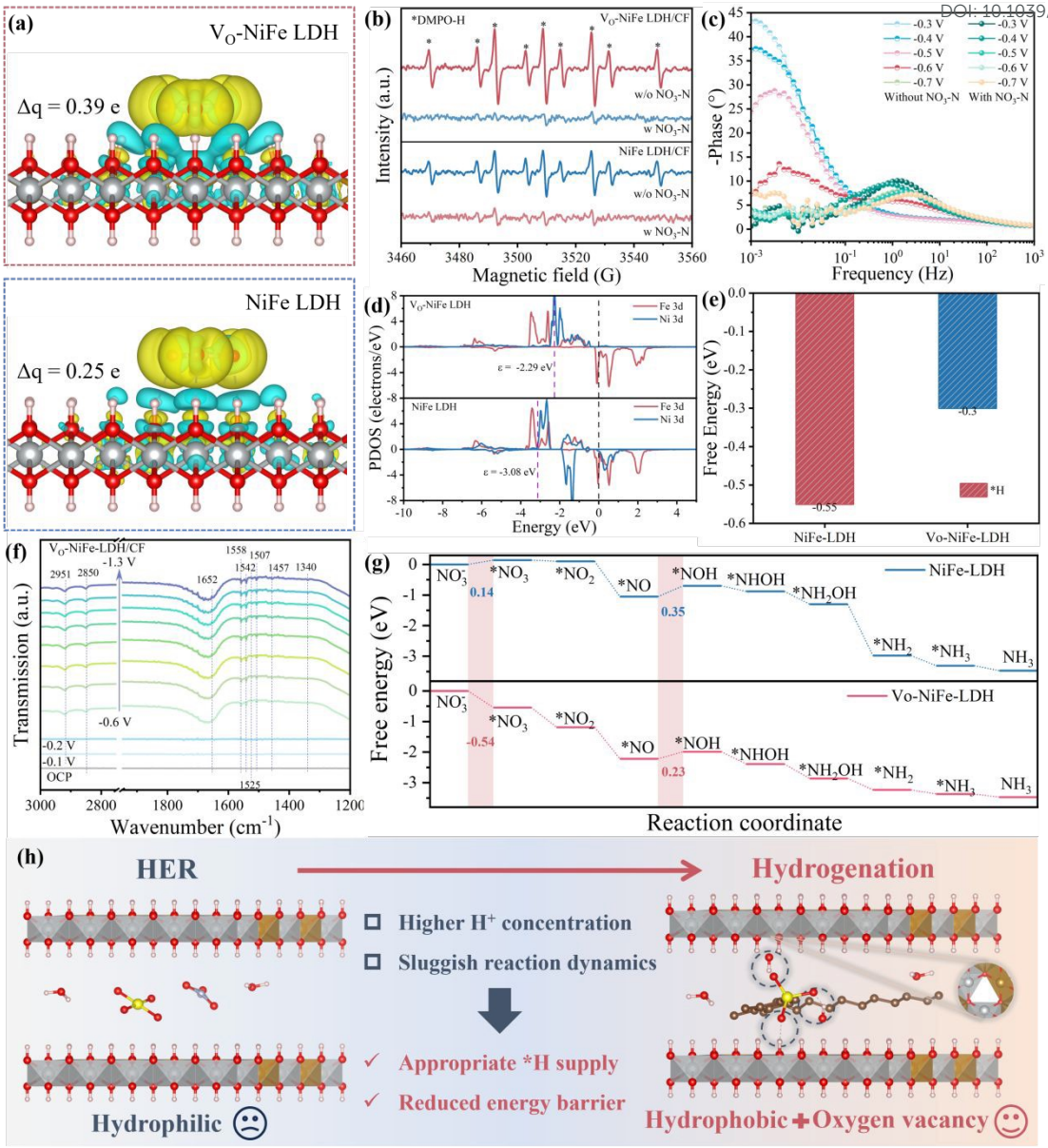

Fig. 4 (a) The charge density difference diagram and Bader charge of NO_3^- adsorption on the V_O-NiFe-LDH and NiFe-LDH, (b) EPR spectra of DMPO-*H during the electrocatalysis process (c) The potential-dependent Bode plots of V_O-NiFe-LDH/CF (d) The PDOS of d-bands, (e) The adsorption free energy of H and (f) In situ FTIR spectra of V_O-NiFe-LDH/CF, (g) The Gibbs free energy change of the NO_3RR over NiFe-LDH and V_O-NiFe-LDH (where * denotes the active site on the catalyst surface). (h) Schematic diagram of enhanced electroreduction ability of low-concentration nitrate over V_O-NiFe-LDH/CF.

3.4 The application potential of V_O-NiFe-LDH/CF

For further investigate the practicability of V_O-NiFe-LDH/CF, a series of electrochemical nitrate reduction experiments were conducted under various operational parameters, including SDBS dosage of electrodeposition process, working current density, initial pH, initial NO_3^--N concentration and different interfering ions. As shown in Fig. 5a, 5b and S27, S28, both NO_3^--N removal efficiency and NH_4^+-N generation ratio increased significantly with increasing SDBS

concentration and working current density. Then, the energy utilization efficiency of the nitrate-to-ammonia process on V_O-NiFe-LDH/CF under different working current densities was calculated [52, 53]. As shown in Fig. S29, the energy utilization efficiency of the nitrate-to-ammonia process on V_O-NiFe-LDH/CF exhibited a gradual increase with increasing current density, reaching a maximum of 42.8% at 10 mA·cm^{-2}. A decrease in energy utilization efficiency was observed at 20 mA·cm^{-2}, which can attributed to increased HER via Tafel or Heyrovsky mechanisms at higher current densities, resulting in a more negative cathodic potential and reduced Faradaic efficiency for nitrate reduction [54]. Therefore, a working current density of 10 mA·cm^{-2} was identified for subsequent electrolysis experiments to balance energy efficiency and nitrate removal performance. In addition, both NO_3^--N removal efficiency and NH_4^+-N generation ratio remain above 90% as the initial pH increases from 5 to 9, indicating the robust applicability of the nitrate-to-ammonia process on V_O-NiFe-LDH/CF across a broader initial pH range (Fig. 5c and S30). As shown in Fig. 5d and S31, electrolysis experiments conducted at varying initial NO_3^--N concentrations (25-100 mg · L^{-1}) revealed that NO_3^--N removal capacity decreased from 96.8% to 58% with increasing initial NO_3^--N concentration. This observation can be attributed to the saturation of active sites on V_O-NiFe-LDH/CF, which limits nitrate adsorption and activation. These results indicat that the V_O-NiFe-LDH/CF cathode is preferentially effective for low-concentration nitrate-to-ammonia conversion in this system. Although the activity of V_O-NiFe-LDH/CF was suppressed at higher NO_3^--N concentrations, ammonia remained high as the dominant product, highlighting its potential for direct application in low-concentration nitrate wastewater treatment. Considering the effects of various constituents in real wastewater [55], electrolysis tests were conducted at the V_O-NiFe-LDH/CF cathode with different interfering ions at various concentrations. These results demonstrate minimal impact on catalytic performance (efficiency and selectivity) in this system, indicating the excellent stability of V_O-NiFe-LDH/CF for nitrate removal and ammonia conversion (Fig. 5 e-h).

Indeed, ammonia recovery at low concentrations may lack economic feasibility compared to high-concentration recovery processes [56]. The treatment strategies for nitrate wastewater across different concentration ranges require in-depth consideration of “waste-to-wealth” and “waste-to-health” principles. Therefore, the subsequent conversion of generated NH_4^+-N to harmless N_2 assisted by chloride ion in wastewater aligns with human health and ecological sustainability goals [57]. The electrocatalytic performance of V_O-NiFe-LDH/CF was evaluated under different Cl^- concentrations, as presented in Fig. S32. The Cl^- addition significantly improves N_2 selectivity, which reaches 98.7% at a Cl^- concentration of 1.5 g·L^{-1} under optimal conditions. In addition, the reaction was conducted under weakly alkaline conditions (pH 8–9), which has been demonstrated to effectively suppress the formation of highly toxic chloramines and favor their complete oxidation

to N_2 through breakpoint chlorination [58, 59]. Furthermore, the treatment ability of V_O-NiFe-LDH/CF for practical industrial nitrate-wastewater was evaluated at an initial total nitrogen (TN) concentration of 114.7 mg·L^{-1} (Fig. 5i), and the water quality parameters provided in Table S1. The TN was reduced to blow 7 mg·L^{-1} through the synergistic effect of nitrate-to-ammonia conversion at the cathode and active chlorine species oxidation at the anode, achieving a TN concentration below the World Health Organization (WHO) emission limit standard [60]. Moreover, Ca^{2+}, Mg^{2+} and chemical oxygen demand (COD) were efficiently removed during nitrate elimination, accompanied by significant chromaticity reduction in treated wastewater compared to the original sample (Fig. S33). Notably, V_O-NiFe-LDH/CF demonstrates a remarkable reduction in energy consumption for nitrate treatment (2.08 kWh/mol) compare with other electrodes, as shown in Table S2.

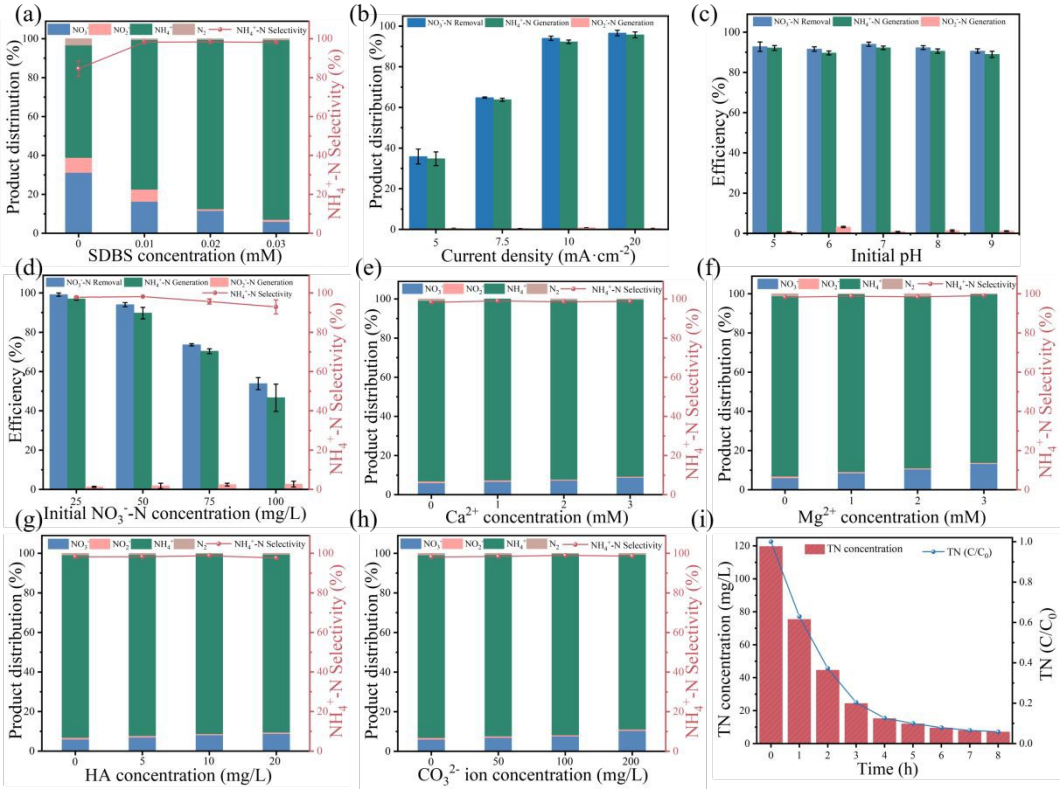

Fig. 5 (a-h) The effect of different operating parameter and interfering ions for electrochemical nitrate-to-ammonia by V_O-NiFe-LDH/CF. (i) Total nitrogen (TN) removal of practical industrial wastewater obtained by V_O-NiFe-LDH/CF.

4. Conclusion

In summary, this work presents a hydrophobic NiFe-LDH electrode by in-situ electrochemical intercalation of SDBS, different of traditional intercalation by ion-exchange method is that the V_O-NiFe-LDH/CF not only retains the hydrophobic property of SDBS but also induces the rich oxygen vacancies. Structural characterization confirmed the successful synthesis of oxygen vacancy-rich, moderately hydrophobic LDH nanoflowers self-grown on copper foam. Electrochemical tests revealed that the V_O-NiFe-LDH/CF accelerates the charge transfer kinetics. The V_O-NiFe-LDH/CF

DOI: 10.1039/D6SC02057G

electrode exhibited a NO_3^--N removal efficiency of 96.8% and ammonia selectivity of 96% under an initial NO_3^--N conditions of 50 mg L^{-1}, which is 2.1-fold higher than that of NiFe-LDH/CF. The enhanced nitrate electroreduction performance can be attributed to the optimized local electron structure and suppressed HER under low-concentration nitrate wastewater conditions. The hydrophobic surface suppresses the HER side reaction through repelling water molecules, while the introduction of oxygen vacancies modulates the local charge distribution of NiFe-LDH and reduced energy barrier of hydrogenation. The Bode phase plots and EPR spectra show that V_O-NiFe-LDH/CF maintains a good balance between generation and consumption of *H. Density functional theory (DFT) calculations revealed that the introduction of oxygen vacancies results in an optimized d-band center, enhanced nitrate adsorption and reduced energy barrier for the rate-determining step (*NO to *NOH). Furthermore, the V_O-NiFe-LDH/CF electrode demonstrated outstanding long-term stability and robust anti-interference performance in cyclic durability tests and practical industrial wastewater treatment. This study provides a novel avenue to synthesis electrodes to realize the efficient treatment of low-concentration nitrate wastewater.

View Article Online
DOI: 10.1039/D6SC02057G

Acknowledgment

This research is financed by the National Natural Science Foundation of China (No. 52070098, 52570084 & 52000104), the Jiangsu Province Carbon Peak Carbon Neutral Technology Innovation special fund project (BE2022861) and the Youth Science and Technology Talent Lifting Project of Jiangsu Province (TJ-2023-099), the Natural Science Foundation of Shanghai (Grant No. 25ZR1402228), the China Postdoctoral Science Foundation under Grant Number 2025M771245, and the Postdoctoral Fellowship Program of CPSF under Grant Number GZC20241003.

Supplementary material

Additional experimental details including electrochemical measurements, DFT calculations, and catalyst characterizations including SEM, XPS, etc.

CRediT authorship contribution statement

Zhifeng Gao: Formal analysis, Investigation, Methodology, Writing – original draft. Jianxing Liang: Formal analysis, Investigation. Mingdi Sun: Formal analysis, Investigation. Xu Yin: Investigation, Methodology, Supervision. Haojie Ling, Methodology. Jiaxiu Wang, Methodology. Kan Li: Funding acquisition, Writing–review & editing. Kajia Wei: Funding acquisition, Supervision, Writing–review & editing. Weiqing Han: Funding acquisition, Supervision.

View Article Online
DOI: 10.1039/D6SC02057G

References

1. K. Dong, S. Han, Y. Li, et al., "Testing, quantification, in situ characterization and calculation simulation for electrocatalytic nitrate reduction," Nature Protocols, (2025), https://doi.org/10.1038/s41596-025-01289-8.

2. P. H. van Langevelde, I. Katsounaros.M. T. M. Koper, "Electrocatalytic nitrate reduction for sustainable ammonia production," Joule, 5 (2) (2021): 290-294, ttps://doi.org/10.1016/j.joule.2020.12.025.

3. A. Seijas-Da Silva, A. Hartert, V. Oestreicher, et al., "Scalable synthesis of NiFe-layered double hydroxide for efficient anion exchange membrane electrolysis," Nature Communications, 16 (1) (2025): 6138, https://doi.org/10.1038/s41467-025-61356-2.

4. G. Fan, F. Li, D. G. Evans, et al., "Catalytic applications of layered double hydroxides: recent advances and perspectives," Chemical Society Reviews, 43 (20) (2014): 7040-7066, https://doi.org/10.1039/C4CS00160E.

5. K. Wang, R. Mao, R. Liu, et al., "Intentional corrosion-induced reconstruction of defective NiFe layered double hydroxide boosts electrocatalytic nitrate reduction to ammonia," Nature Water, 1 (12) (2023): 1068-1078, https://doi.org/10.1038/s44221-023-00169-3.

6. J. Li, N. Zhao, X. Liu, et al., "Two-dimensional layered double hydroxides for advanced sensors," Coordination Chemistry Reviews, 523 (2025): 216262, https://doi.org/10.1016/j.ccr.2024.216262.

7. R. Yi, X. Mo, H. T. Yau, et al., "Interlayer expansion enables electrochemical domino C–N coupling for formaldoxime formation in aqueous media," Journal of the American Chemical Society, (2025), https://doi.org/10.1021/jacs.5c08836.

8. Y. Wang, Q. Pan, Y. Qiao, et al., "Layered Metal Oxide Nanosheets with Enhanced Interlayer Space for Electrochemical Deionization," Advanced Materials, 35 (15) (2023): 2210871, ttps://doi.org/10.1002/adma.202210871.

9. S. Xu.C. Liu, "Interface engineering gives enhanced selectivity in electrochemical nitrogen reduction reaction," Chem Catalysis, 2 (8) (2022): 1841-1843, https://doi.org/10.1016/j.checat.2022.07.006.

10. J. Zhang, B. Zhao, W. Liang, et al., "Three-phase electrolysis by gold nanoparticle on hydrophobic interface for enhanced electrochemical nitrogen reduction reaction," Advanced Science, 7 (22) (2020): 2002630, https://doi.org/10.1002/advs.202002630.

11. Y. Xiong, Y. Wang, J. Zhou, et al., "Electrochemical nitrate reduction: ammonia synthesis and the beyond," Advanced Materials, 36 (17) (2024): 2304021, https://doi.org/10.1002/adma.202304021.

12. W.-J. Sun, H.-Q. Ji, L.-X. Li, et al., "Built-in electric field triggered interfacial accumulation effect for efficient nitrate removal at ultra-low concentration and electroreduction to ammonia," Angewandte Chemie International Edition, 60 (42) (2021): 22933-22939, https://doi.org/10.1002/anie.202109785.

13. A. Li, Q. Cao, G. Zhou, et al., "Three-phase photocatalysis for the enhanced selectivity and activity of CO_2 reduction on a hydrophobic surface," Angewandte Chemie International Edition, 58 (41) (2019): 14549-14555, https://doi.org/10.1002/anie.201908058.

14. Y. Peng, L. Wang, Q. Luo, et al., "Molecular-level insight into how hydroxyl groups boost catalytic activity in CO_2 hydrogenation into methanol," Chem, 4 (3) (2018): 613-625, https://doi.org/10.1016/j.chempr.2018.01.019.

15. X. Wang, R. Zhang, C. Ma, et al., "Surface hydrophobic modification of MXene to promote the electrochemical conversion of N_2 to NH_3," Journal of Energy Chemistry, 87 (2023): 439-449, https://doi.org/10.1016/j.jechem.2023.08.043.

16. Y. Song, C. B. Musgrave, J. Su, et al., "Efficient CO_2-to-methanol electrocatalysis in acidic media via microenvironment-tuned cobalt phthalocyanine," Nature Nanotechnology, (2025), https://doi.org/10.1038/s41565-025-02059-z.

17. Y. Liu, Y. Zheng, Y. Ren, et al., "Selective nitrate electroreduction to ammonia on CNT electrodes with controllable interfacial wettability," Environmental Science & Technology, 58 (16) (2024): 7228-7236, https://doi.org/10.1021/acs.est.4c01464.

18. D. Xu, Y. Liu, Y. Zhang, et al., "Fabrication of pyramid-$BiVO_4$/CdSe composite with controlled surface oxygen vacancies boosting efficient carriers' separation for photocathodic protection," Chemical Engineering Journal, 393 (2020): 124693, https://doi.org/10.1016/j.cej.2020.124693.

19. Y. Gao, K. Wang, C. Xu, et al., "Enhanced electrocatalytic nitrate reduction through phosphorus-vacancy-mediated kinetics in heterogeneous bimetallic phosphide hollow nanotube array," Applied Catalysis B: Environmental, 330 (2023): 122627, https://doi.org/10.1016/j.apcatb.2023.122627.

20. Y. Xu, C. Cheng, J. Zhu, et al., "Sulphur-boosted active hydrogen on copper for enhanced electrocatalytic nitrate-to-ammonia selectivity," Angewandte Chemie International Edition, 63 (16) (2024): e202400289, https://doi.org/10.1002/anie.202400289.

21. Y. Wu, M. Song, Y.-C. Huang, et al., "Promoting surface reconstruction of NiFe layered double hydroxides via intercalating $[Cr(C_2O_4)_3]^{3-}$ for enhanced oxygen evolution," Journal of Energy Chemistry, 74 (2022): 140-148, https://doi.org/10.1016/j.jechem.2022.06.045.

22. H. Bai, L. Liang, S. Chen, et al., "Modulating electronic structure of NiFe layered double hydroxide membrane by interlayer-confinement for enhanced water decontamination," Applied Catalysis B: Environment and Energy, 363 (2025): 124790, https://doi.org/10.1016/j.apcatb.2024.124790.

23. J. Zhang, X. Zhang, Z. Ma, et al., "POM-intercalated NiFe-LDH as enhanced OER catalyst for highly efficient and durable water electrolysis at ampere-scale current densities," ACS Catalysis, 15 (8) (2025): 6486-6496, https://doi.org/10.1021/acscatal.5c00448.

24. X. Lin, Z. Wang, S. Cao, et al., "Bioinspired trimesic acid anchored electrocatalysts with unique static and dynamic compatibility for enhanced water oxidation," Nature Communications, 14 (1) (2023): 6714, https://doi.org/10.1038/s41467-023-42292-5.

25. Y. Liu, G. Chen, R. Ge, et al., "Construction of CoNiFe trimetallic carbonate hydroxide hierarchical hollow

View Article Online
DOI: 10.1039/D6SC02057G

microflowers with oxygen vacancies for electrocatalytic water oxidation," Advanced Functional Materials, 32 (32) (2022): 2200726, https://doi.org/10.1002/adfm.202200726.

26. K. Liang, Z. Dou, Y. Zhang, et al., "Preparation of one-step organic anion-modified MgAl-LDH films under mild conditions for Mg alloy corrosion protection," Journal of Materials Science, 58 (43) (2023): 16841-16854, https://doi.org/10.1007/s10853-023-09070-6.

27. D.-Y. Wang, F. R. Costa, A. Vyalikh, et al., "One-step synthesis of organic LDH and its comparison with regeneration and anion exchange method," Chemistry of Materials, 21 (19) (2009): 4490-4497, https://doi.org/10.1021/cm901238a.

28. Y. Sun, K. Fan, J. Li, et al., "Boosting electrochemical oxygen reduction to hydrogen peroxide coupled with organic oxidation," Nature Communications, 15 (1) (2024): 6098, https://doi.org/10.1038/s41467-024-50446-2.

29. D. Chen, S. Zhang, X. Bu, et al., "Synergistic modulation of local environment for electrochemical nitrate reduction via asymmetric vacancies and adjacent ion clusters," Nano Energy, 98 (2022): 107338, https://doi.org/10.1016/j.nanoen.2022.107338.

30. J. Bao, X. Zhang, B. Fan, et al., "Ultrathin spinel-structured nanosheets rich in oxygen deficiencies for enhanced electrocatalytic water oxidation," Angewandte Chemie International Edition, 54 (25) (2015): 7399-7404, https://doi.org/10.1002/anie.201502226.

31. L. Liu, Q. Liu, Y. Wang, et al., "Nonradical activation of peroxydisulfate promoted by oxygen vacancy-laden NiO for catalytic phenol oxidative polymerization," Applied Catalysis B: Environmental, 254 (2019): 166-173, https://doi.org/10.1016/j.apcatb.2019.04.094.

32. G. Long, A. Wang, X. Liu, et al., "Tunable oxygen vacancy clusters enhanced catalytic activity of CeO_2 nanorods on CO_2 cycloaddition," Angewandte Chemie International Edition, 64 (34) (2025): e202508217, ttps://doi.org/10.1002/anie.202508217.

33. K. Flores, D. Varda, N. Hald, et al., "Engineering copper supported mixed manganese oxides as selective bimetallic electrocatalyst for nitrate to ammonia conversion at environmentally relevant concentrations," Applied Catalysis B: Environment and Energy, 362 (2025): 124682, https://doi.org/10.1016/j.apcatb.2024.124682.

34. K. Zhang, X. Zhu, N. Graham, et al., "Identification of dual center in self-supported Pd-dispersed Cu_2O/Cu nanowire arrays featuring cooperativity for durable electrochemical removal of low-concentration nitrate," Applied Catalysis B: Environment and Energy, 384 (2026): 126166, https://doi.org/10.1016/j.apcatb.2025.126166.

35. J. Zhang, L. Liu, N. Hu, et al., "Accelerating proton coupled electron transfer by confined Cu-Ni bimetallic clusters for boosting electrochemical hydrodeoxygenation of nitrate," Applied Catalysis B: Environment and Energy, 371 (2025): 125195, https://doi.org/10.1016/j.apcatb.2025.125195.

36. W. Kang, L. Yan, J. Tang, et al., "Electrochemical activation of graphite electrode for nitrate reduction: Energetic performance and application potential," Applied Catalysis B: Environmental, 329 (2023): 122553, https://doi.org/10.1016/j.apcatb.2023.122553.

37. R. Mao, H. Zhu, K. Wang, et al., "Selective conversion of nitrate to nitrogen gas by enhanced electrochemical process assisted by reductive Fe(II)-Fe(III) hydroxides at cathode surface," Applied Catalysis B: Environmental, 298 (2021): 120552, https://doi.org/10.1016/j.apcatb.2021.120552.

38. Y.-J. Shih, Z.-L. Wu, C.-Y. Lin, et al., "Manipulating the crystalline morphology and facet orientation of copper and copper-palladium nanocatalysts supported on stainless steel mesh with the aid of cationic surfactant to improve the electrochemical reduction of nitrate and N_2 selectivity," Applied Catalysis B: Environmental, 273 (2020): 119053, https://doi.org/10.1016/j.apcatb.2020.119053.

39. G. A. Cerrón-Calle, A. S. Fajardo, C. M. Sánchez-Sánchez, et al., "Highly reactive Cu-Pt bimetallic 3D-electrocatalyst for selective nitrate reduction to ammonia," Applied Catalysis B: Environmental, 302 (2022): 120844, https://doi.org/10.1016/j.apcatb.2021.120844.

40. L. Cai, Y. Liu, J. Zhang, et al., "Unveiling the geometric site dependent activity of spinel Co_3O_4 for electrocatalytic chlorine evolution reaction," Journal of Energy Chemistry, 92 (2024): 95-103, https://doi.org/10.1016/j.jechem.2023.12.002.

41. T. Jin, J. Wang, Y. Gong, et al., "Mechanochemical-tuning size dependence of iridium single atom and nanocluster toward highly selective ammonium production," Chem Catalysis, 3 (1) (2023): 100477, https://doi.org/10.1016/j.checat.2022.11.016.

42. S. Liang, X. Teng, H. Xu, et al., "H* Species Regulation by Mn-$Co(OH)_2$ for Efficient Nitrate Electro-reduction in Neutral Solution," Angewandte Chemie International Edition, 63 (11) (2024): e202400206, https://doi.org/10.1002/anie.202400206.

43. Z. Fan, C. Cao, X. Yang, et al., "Interfacial Electronic Interactions Promoted Activation for Nitrate Electroreduction to Ammonia over Ag-Modified Co_3O_4," Angewandte Chemie International Edition, 63 (44) (2024): e202410356, https://doi.org/10.1002/anie.202410356.

44. J. Guan, L. Cai, W. Li, et al., "Boosting nitrate electroreduction to ammonia on atomic Ru-Co pair sites in hollow spinels," Applied Catalysis B: Environment and Energy, 358 (2024): 124387, https://doi.org/10.1016/j.apcatb.2024.124387.

45. J. Liang, K. Li, F. Shi, et al., "Constructing high-performance cobalt-based environmental catalysts from spent lithium-ion batteries: unveiling overlooked roles of copper and aluminum from current collectors," Angewandte Chemie International Edition, 63 (32) (2024): e202407870, https://doi.org/10.1002/anie.202407870.

46. H. Liu, S. Jia, L. Wu, et al., "Circumventing scaling relations via gradient orbital coupling promotes ammonia electrosynthesis on cobalt catalyst," Angewandte Chemie International Edition, 64 (32) (2025): e202510478, https://doi.org/10.1002/anie.202510478.

47. R. Javed, B. Zhao, Z. Zafar, et al., "Pd single-atoms doped Cu_3P quantum dots with moderately optimized H* sorption behaviors for actualizing the multifunctional "formaldehyde-nitrate" galvanic system," Advanced Materials, 37 (45) (2025): e12332, https://doi.org/10.1002/adma.202512332.

48. M. Xu, L. Huang, S. Zhang, et al., "Modulating electron transfer from palladium to spinel cobalt oxide nanofibers for high-efficiency hydrazine oxidation-assisted energy-saving nitrate-to-ammonia conversion," Advanced Functional Materials, 16 (2026): e75722, https://doi.org/10.1002/adfm.75722.

49. Y. Yao, S. Zhu, H. Wang, et al., "A spectroscopic study on the nitrogen electrochemical reduction reaction on gold and platinum surfaces," Journal of the American Chemical Society, 140 (4) (2018): 1496-1501, https://doi.org/10.1021/jacs.7b12101.

50. J.-Y. Fang, Q.-Z. Zheng, Y.-Y. Lou, et al., "Ampere-level current density ammonia electrochemical synthesis using CuCo nanosheets simulating nitrite reductase bifunctional nature," Nature Communications, 13 (1) (2022): 7899, https://doi.org/10.1038/s41467-022-35533-6.

51. B. Huang, J. Yan, Z. Li, et al., "Anode-electrolyte interfacial acidity regulation enhances electrocatalytic performances of alcohol oxidations," Angewandte Chemie International Edition, 63 (40) (2024): e202409419, https://doi.org/10.1002/anie.202409419.

52. L. Szpyrkowicz, S. Daniele, M. Radaelli, et al., "Removal of NO_3^- from water by electrochemical reduction in different reactor configurations," Applied Catalysis B: Environmental, 66 (1) (2006): 40-50, https://doi.org/10.1016/j.apcatb.2006.02.020.

53. L. Su, K. Li, H. Zhang, et al., "Electrochemical nitrate reduction by using a novel Co_3O_4/Ti cathode," Water Research, 120 (2017): 1-11, https://doi.org/10.1016/j.watres.2017.04.069.

54. R. Mao, C. Huang, X. Zhao, et al., "Dechlorination of triclosan by enhanced atomic hydrogen-mediated electrochemical reduction: Kinetics, mechanism, and toxicity assessment," Applied Catalysis B: Environmental, 241 (2019): 120-129, https://doi.org/10.1016/j.apcatb.2018.09.013.

55. J. Fan, L. K. Arrazolo, J. Du, et al., "Effects of ionic interferents on electrocatalytic nitrate reduction: mechanistic insight," Environmental Science & Technology, 58 (29) (2024): 12823-12845, https://doi.org/10.1021/acs.est.4c03949.

56. H. Huang, K. Peramaiah.K.-W. Huang, "Rethinking nitrate reduction: redirecting electrochemical efforts from ammonia to nitrogen for realistic environmental impacts," Energy & Environmental Science, 17 (8) (2024): 2682-2685, https://doi.org/10.1039/D4EE00222A.

57. P. Jiang, T. Zhou, J. Bai, et al., "Nitrogen-containing wastewater fuel cells for total nitrogen removal and energy recovery based on Cl•/ClO• oxidation of ammonia nitrogen," Water Research, 235 (2023): 119914, https://doi.org/https://doi.org/10.1016/j.watres.2023.119914.

58. M. Duca.M. T. M. Koper, "Powering denitrification: the perspectives of electrocatalytic nitrate reduction," Energy & Environmental Science, 5 (12) (2012): 9726-9742, https://doi.org/10.1039/C2EE23062C.

59. A. G. Vlyssides, P. K. Karlis, N. Rori, et al., "Electrochemical treatment in relation to pH of domestic wastewater using Ti/Pt electrodes," Journal of Hazardous Materials, 95 (1) (2002): 215-226, https://doi.org/10.1016/S0304-3894(02)00143-7.

60. J. Chen, H. Wu, H. Qian, et al., "Assessing nitrate and fluoride contaminants in drinking water and their health risk of rural residents living in a semiarid region of northwest china," Exposure and Health, 9 (3) (2017): 183-195, https://doi.org/10.1007/s12403-016-0231-9.

Data are available from the corresponding author upon reasonable request

View Article Online
DOI: 10.1039/D6SC02057G